LITHOS 398-399 (2021) 106337

Contents lists available at ScienceDirect

LITHOS

journal homepage: www.elsevier.com/locate/lithos

Research Article

# Late Triassic dacites from Well NK-1 in the Nansha Block: Constraints on the Mesozoic tectonic evolution of the southern South China Sea margin

Xiu-Quan Miao [a,b,c,d], Xiao-Long Huang [a,b,d,*], Wen Yan [d,e], Fan Yang [a,b,d], Wan-Feng Zhang [a,b,d], Yu-Xin Cai [a,b,c,d], Yang Yu [a,b,d], Peng-Li He [a,b,d]

[a] State Key Laboratory of Isotope Geochemistry, Guangzhou Institute of Geochemistry, Chinese Academy of Sciences, Guangzhou 510640, China
[b] CAS Center for Excellence in Deep Earth Science, Guangzhou, 510640, China
[c] University of Chinese Academy of Sciences, Beijing, 100049, China
[d] Southern Marine Science and Engineering Guangdong Laboratory (Guangzhou), Guangzhou 511458, China
[e] CAS Key Laboratory of Ocean and Marginal Sea Geology, South China Sea Institute of Oceanology, Innovation Academy of South China Sea Ecology and Environmental Engineering, Chinese Academy of Sciences, Guangzhou 510301, China

ARTICLE INFO

*Keywords:*
A-type granite
Subduction
Continental margin
Paleogeographic reconstruction
Early Mesozoic
South China Sea

ABSTRACT

Identifying whether and when the southern continental margin of the South China Sea (SCS) was part of the South China Block (SCB) is important for Mesozoic–Cenozoic paleogeographic reconstructions of Southeast Asia. In this paper, we present geochronological and geochemical data for dacites from Well NK-1 in the Nansha Block (Dangerous Grounds) of the southern SCS margin to investigate their petrogenesis and tectonic affinity. Zircon U—Pb and $^{40}Ar/^{39}Ar$ datings show that these dacites formed during the Late Triassic (218–217 Ma). The dacites have high total alkali ($K_2O + Na_2O$ = 7.39–8.42 wt%) and relatively low CaO contents (1.87–3.38 wt%), and show geochemical affinities with A-type granites, with high Zr saturation temperatures (806–855 °C), $FeO^{Tot}$/MgO ratios (5.22–7.48), Zr + Nb + Ce + Y contents (530–680 ppm) and 10,000 × Ga/Al values (2.40–2.94), and relatively low A/CNK values (0.86–1.04). The primitive magma for the dacites was likely generated by partial melting of ancient crustal materials. Late Triassic dacites in the Nansha Block and Triassic A-type granites in the SCB formed in an extensional setting at the continental margin of the SCB. This setting was probably related to the Paleo-Pacific plate subduction that restarted prior to the Early Triassic. Therefore, the southern SCS margin was part of the SCB continental margin during the early Mesozoic, which provides more detailed insights into the paleogeography of SE Asia since the Mesozoic.

## 1. Introduction

The South China Sea (SCS) is located at the junction of the Eurasian, Pacific, and Indo-Australian plates, and regarded part of the southward extension of the South China Block (SCB; Fig. 1a). The large positive magnetic anomalies and arc-related igneous rocks along the continental margin of the SCB suggest a Mesozoic volcanic arc (i.e., subduction zone) existing along the southeastern margin of the SCB (e.g., Suo et al., 2019; Wan et al., 2017). The Mesozoic silicic–intermediate intrusive and volcanic rocks drilled at sites along the northern continental margin of the SCS likely formed in a continental arc setting (Xu et al., 2017) and are geochemically correlated with those widely distributed in the SCB (Fig. 1a). This indicates that the northern SCS had a genetic relationship with the SCB during the Mesozoic. In the Late Cretaceous, westward subduction of the Paleo-Pacific plate beneath the SCB ceased, and was followed by opening of the SCS in the Oligocene–early Miocene (Briais et al., 1993; Huang et al., 2013). This resulted in the Nansha (Dangerous Grounds), Reed Bank, Palawan, and Mindoro blocks being distributed in their present-day positions along the southern continental margin of the SCS (Fig. 1a). Thus, an important question is whether the southern SCS margin was also connected to the SCB margin before rifting. Some geological and geophysical surveys have been conducted on the southern SCS margin. Suggate et al. (2014) and Shao et al. (2017) proposed that the Palawan Block was adjacent to the SCB during the late Mesozoic, based on heavy mineral analysis and U—Pb dating of detrital zircons from sedimentary rocks. The Reed Bank Block was also presumably

* Corresponding author at: State Key Laboratory of Isotope Geochemistry, Guangzhou Institute of Geochemistry, Chinese Academy of Sciences, Guangzhou 510640, China.
*E-mail address:* xlhuang@gig.ac.cn (X.-L. Huang).

https://doi.org/10.1016/j.lithos.2021.106337
Received 29 January 2021; Received in revised form 17 June 2021; Accepted 27 June 2021
Available online 30 June 2021

distributed along the margin of the SCB, because these areas have similar Mesozoic strata and gravity anomalies (Cullen et al., 2010; Kudrass et al., 1986). Although seismic data have revealed that the lithosphere thickness of the Nansha Block is similar to that of the SCB (Dong et al., 2019), it is still unclear whether the southern SCS was tectonically associated with the SCB during the early Mesozoic. Furthermore, it remains unclear whether the opening of the SCS or the proto-SCS separated the micro-blocks along the southern SCS margin (Wu and Suppe, 2018). It has been proposed that the Palawan Block rifted from the SCB as early as the latest Cretaceous when the proto-SCS formed (e.g., Zahirovic et al., 2014). If so, the Palawan Block should have been located on the southern side of the proto-SCS in the Late Cretaceous. However, it has also been proposed that the Palawan Block drifted southward in response to the opening of the SCS in the Oligocene (e.g., Hall, 2012). Therefore, identification of the tectonic affinity of the southern SCS continental margin during the early Mesozoic is key for understanding the tectonic evolution and paleogeography of Southeast Asia.

The SCB comprises the Yangtze Block in the northwest and the Cathaysia Block in the southeast. The Cathaysia Block is further divided into interior and coastal parts by the NNE–SSW-trending Zhenghe–Dapu Fault (Fig. 1a). The SCB contains widespread Mesozoic igneous rocks that formed over three main intervals: the early Mesozoic or Indosinian (Triassic), the early Yanshanian (Jurassic), and the late Yanshanian (Cretaceous) (e.g., Zhou et al., 2006). It is generally accepted that these Mesozoic igneous rocks were related to the subduction of the Paleo-Pacific plate, although it remains unclear how and when the Paleo-Pacific plate subduction affected the continental margin of the SCB. The subduction might have begun in the Triassic (e.g., Li and Li, 2007), Early Jurassic (e.g., Li et al., 2018 and references therein), Middle Jurassic (e.g., Zhou and Li, 2000), or Early Cretaceous (Chen et al., 2008). Thus, whether the Triassic igneous rocks are related to the Paleo-Pacific plate subduction is a fundamental issue for understanding the early Mesozoic evolution of the continental margin of the SCB. Triassic granites occur mainly in the interior of the SCB, and are predominantly peraluminous S-type (>90%) and minor I- and A-type granites (Zhou et al., 2006). These S- and I-type granites may be related to compressional tectonism associated with the collision between the SCB and Indochina Block (e.g., Wang et al., 2007; Zhao et al., 2013), the North China Block (e.g., Zhao et al., 2013), or the Paleo-Pacific Plate (e.g., Sun et al., 2011; Wang et al., 2005). Some Triassic A-type granites and Late Permian-Early Triassic syenites crop out along the NNE–SSW-trending Zhenghe–Dapu Fault (Fig. 1a), which are indicative of an extensional tectonic setting (Sun et al., 2011; Wang et al., 2005; Zhao et al., 2013).

Here we present zircon U—Pb and $^{40}Ar/^{39}Ar$ dating results, and whole-rock geochemical and Sr–Nd–Hf–Pb isotopic and mineral compositional data for Triassic dacites from the Well NK-1 (NK-1 drillhole) in the Nansha Block, with aims to investigate their petrogenesis. In addition, comparison with Triassic granites in the Cathaysia Block (Fig. 1a) and other Mesozoic igneous rocks in the surrounding blocks enables us to identify the tectonic affinity of the southern continental margin of the SCS. This is then used to constrain the tectonic evolution of micro-blocks along the southern continental margin of the SCS since the Mesozoic.

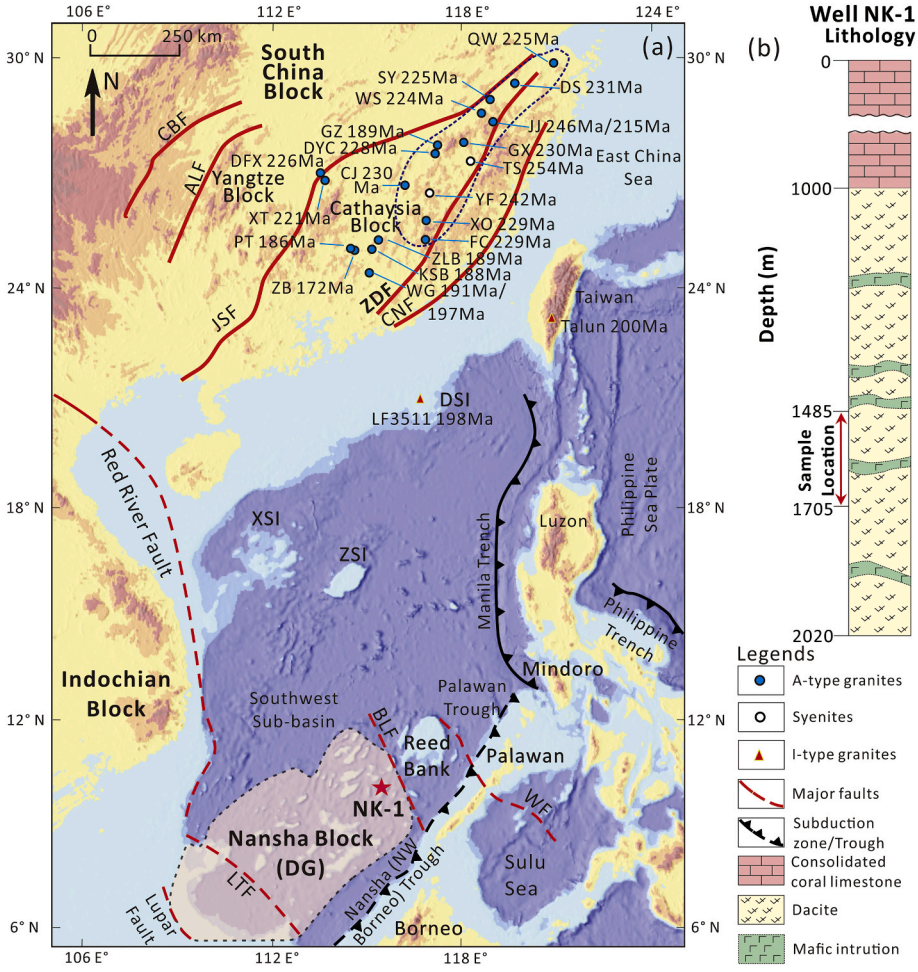


**Fig. 1.** (a) Simplified tectonic outline of the South China Block and South China Sea, showing the locations of Well NK-1 in the Nansha Block and Triassic–Jurassic A-type granites and Late Permian–Early Triassic syenites in the South China Block. (b) The igneous basement lithology of Well NK-1. The ages of granites and syenites are from the references listed in the supporting information of Appendix-2. Abbreviations: Caijiang biotite monzogranite (CJ); Dashuang monzogranite (DS); Dayichang biotite granite (DYC); Defuxian biotite granite (DFX); Fucheng granite (FC); Gaoxi biotite granite (GX); Guangze alkali-feldspar granite and syenogranite (GZ); Jingju syenogranite (JJ); Keshubei granite (KSB); Qiuwang biotite granite (QW); Sheyang syenogranite (SY); Xiaotao monzogranite (XO); Xitian biotite granite (XT); Pitou syenogranite (PT); Tieshan syenite (TS); Wengong hornblende K-feldspar granite (WG); Wenshan biotite monzogranite (WS); Yangfang syenite (YF); Zhaibei K-feldspar granite (ZB) and Zhulanbu biotite granite (ZLB); Anhua–Luocheng Fault (ALF); Balabac Fault (BLF); Changle–Nanao Fault (CNF); Cili–Baojing Fault (CBF); Jiangshan–Shaoxing Fault (JSF); Lizhun–Tinjia Fault (LTF); Qiyueshan Fault (QYF); Wulugen Fault (WF); Xiangfan–Guangji Fault (XGF); Zhenghe–Dapu Fault (ZDF); Dongsha Islands (DSI); Xisha Islands (XSI); Zhongsha Islands (ZSI).

## 2. Geological setting and petrography

### 2.1. Geological setting

The SCS is one of the largest marginal seas in the western Pacific, and is located south of the SCB, north of the Borneo Block, east of the Indochina Block, and west of the Palawan and Mindoro blocks (Fig. 1a). The SCS lithosphere can be divided into three parts: the northern continental margin, oceanic basin, and southern continental margin. There are several micro-blocks within the SCS, including the Zhongsha (Macclesfield Bank), Xisha (Paracel Islands), Dongsha (Pratas Reef), Nansha (Dangerous Grounds and Spratly Islands), and Reed Bank (Liyue Block) blocks (Yan et al., 2011). The Nansha Block is bounded by the southwest sub-basin of the SCS and a NE–SW-trending fault in the northwest, the Lupar Fault in the southwest, and Nansha Trough in the southeast (Fig. 1a). It is generally considered that the blocks surrounding the Nansha Block, such as the Reed Bank, Palawan, and Mindoro blocks, were distributed along the continental margin of the SCB during the Mesozoic. Subsequently, these blocks separated from the continental margin of the SCB and drifted southward to their present position during opening of the SCS in the Cenozoic (e.g., Kudrass et al., 1986; Shao et al., 2017; Suggate et al., 2014).

Widespread Mesozoic igneous rocks crop out in the blocks surrounding the Nansha Block (e.g., Knittel et al., 2010; Suggate et al., 2014). However, there have been no studies of early Mesozoic igneous rocks and their petrogenesis from the Nansha Block. Well NK-1 was drilled in the Nansha Block in the southeastern SCS. The drillhole penetrated thick, consolidated, coralline limestone (~1000 m) and underlying igneous rocks (~1000 m), and had a total length of 2020.2 m (Fig. 1b). The drilled igneous rocks are predominantly dacites, with a small amount of mafic rocks, which intruded the former (Figs. 1b and 2a). The studied dacites were collected at depths of 1485–1705 m (Fig. 1b).

### 2.2. Sample descriptions

The dacites from Well NK-1 are porphyritic and contain abundant phenocrysts, including plagioclase (~30 vol%), biotite (5 vol%), and titanite (5 vol%; Fig. 2). The plagioclase is euhedral–subhedral and variable in grain size (Fig. 2a–b). The titanite is rhombic and euhedral–subhedral (Fig. 2c). Some of the plagioclases and titanites have been epidotized (Fig. 2b). Apatite is common accessory mineral, and some apatites occur as inclusions in phenocrysts of plagioclase, biotite, and titanite (Fig. 2d). The groundmass consists mainly of K-feldspar, quartz, and biotite (Fig. 2d).

## 3. Results

Analytical methods are given in the supporting information of Appendix-1.

### 3.1. Zircon U—Pb and $^{40}Ar/^{39}Ar$ ages

Zircon U—Pb dating results of the selected dacite samples (NK-1-$V_3$–009, NK-1-$V_3$–068, and NK-1-$V_3$–143 from depths of 1512, 1582, and 1695 m, respectively) from Well NK-1 are listed in Supplemental Table 1. The zircons from these samples are generally euhedral and prismatic grains. The zircons exhibit oscillatory zoning in cathodoluminescence (CL) images (Fig. 3a) and have relatively high Th and U contents (43.3–330 and 74.1–473 ppm, respectively), with high Th/U ratios of 0.54–1.01. All three dacite samples have uniform weighted-mean $^{206}Pb/^{238}U$ ages (218 ± 2, 217 ± 2, and 217 ± 2 Ma; Fig. 3b–d),

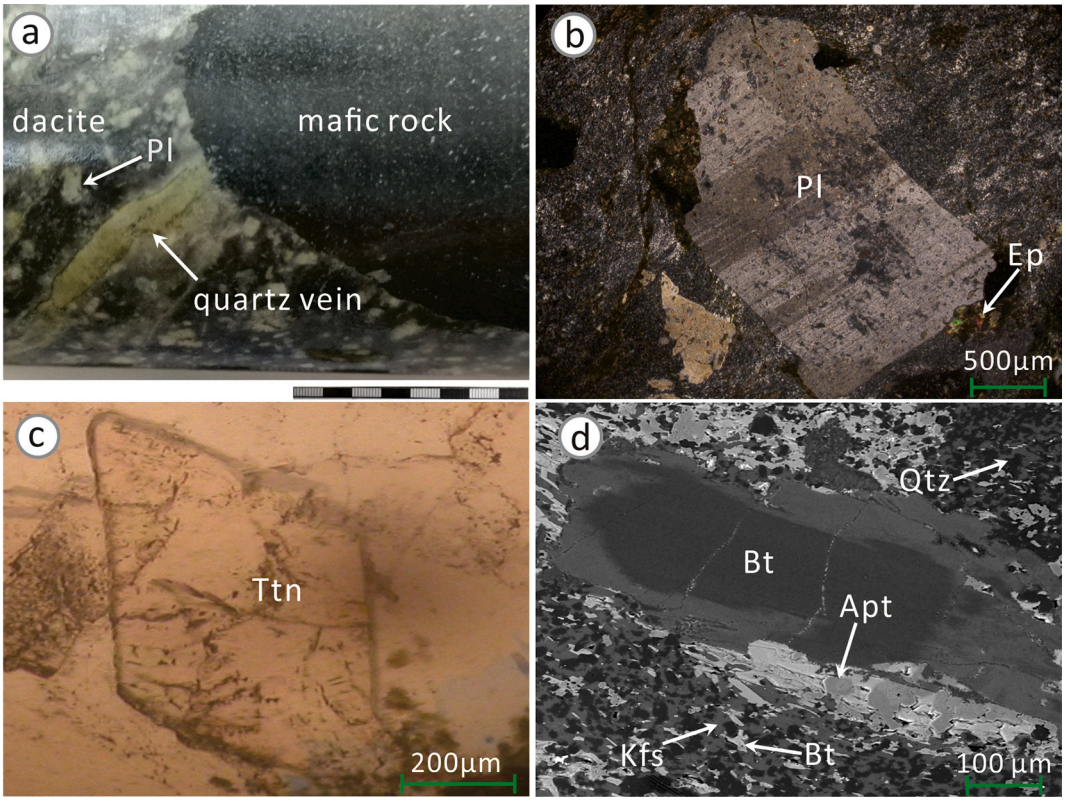


**Fig. 2.** Petrography of dacites from Well NK-1. (a) fine-grained mafic rock cutting porphyritic dacite; (b) plagioclase phenocryst whose rim is epidotized (cross-polarized light); (c) euhedral titanite phenocryst (cross-polarized light); (d) BSE image of a biotite phenocryst containing apatite, with a groundmass consisting mainly of K-feldspar, quartz, and biotite. Abbreviations: apatite (Apt); biotite (Bt); ilmenite (Ilm); K-feldspar (Kfs); plagioclase (Pl); quartz (Qtz); titanite (Ttn); epidotite (Ep).

interpreted as the crystallization age of the dacites in the Nansha Block.

$^{40}Ar/^{39}Ar$ dating results for plagioclase from sample NK-1-$V_3$–068 are listed in Supplemental Table 2, and the age spectrum is shown in Fig. 4. The plateau age is 217 ± 10 Ma (cumulative $^{39}Ar$ released ~50%; Fig. 4), which is consistent with the zircon U—Pb ages (Fig. 3b–d).

### 3.2. Mineral chemistry

The chemical compositions of plagioclase and apatite are listed in Supplemental Tables 3 and 4, respectively. The plagioclase has low CaO (0.02–1.24 wt%) and $K_2O$ (0.02–1.23 wt%) contents, high $Na_2O$ (10.5–11.8 wt%) and $Al_2O_3$ (19.3–22.6 wt%) contents, and high Ab contents of 91–99 mol% (Supplemental Table 3). The apatite is enriched in F (0.92–3.40 wt%), depleted in Cl (0.01–0.08 wt%), and has variable F/Cl ratios (22.9–2006; Supplemental Table 4). The apatites are all fluorapatite.

### 3.3. Whole-rock major and trace element chemistry

Whole-rock major and trace element data are listed in Supplemental Table 5. These samples have loss-on-ignition (LOI) values of 0.98–1.22 wt%, and the major element data were re-calculated on an anhydrous basis.

The studied dacites are silicic in composition and have high $SiO_2$ (65.4–68.1 wt%) and total alkali ($Na_2O + K_2O$ = 7.39–8.42 wt%) contents, relatively low MgO (0.70–1.50 wt%) and $TiO_2$ (0.71–0.98 wt%) contents, and low $Mg^{\#}$ values (19.2–31.7). The rocks are classified as trachydacite–dacite on a total alkalis–silica (TAS) classification diagram (Fig. 5a), and belong to the high-K calc-alkaline and shoshonitic series because of their high $K_2O$ contents (3.41–4.68 wt%; Fig. 5b). The samples have uniform $Al_2O_3$ (14.1–14.6 wt%) and low CaO (1.87–3.38 wt%) contents, and are metaluminous to weakly peraluminous with A/CNK values of 0.86–1.05 (Fig. 5c).

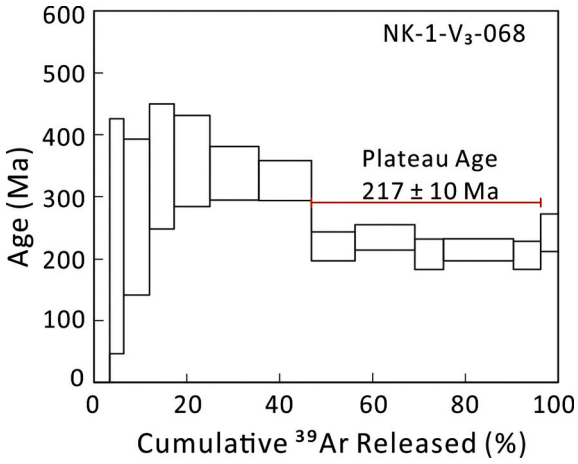


**Fig. 4.** $^{40}Ar/^{39}Ar$ age spectra for dacites from Well NK-1.

The dacites have similar chondrite-normalized rare earth element (REE) patterns, which are characterized by enrichment of light REEs (LREEs) and depletion of heavy REEs (HREEs), with high $(La/Yb)_N$ (7.97–8.64), low $(Gd/Yb)_N$ (1.57–1.71), and marked negative Eu anomalies (δEu = 0.60–0.67; Fig. 6a). On primitive-mantle-normalized multi-element diagrams, all the dacites are enriched in Rb, K, Pb, Th, U, Zr, and Hf, but depleted in Ba, Sr, Nb, Ta, and Ti, and have an affinity with continental crust (Fig. 6b).

### 3.4. Whole-rock Sr–Nd–Pb–Hf isotope data

Whole-rock Sr–Nd–Pb–Hf isotope data are listed in Supplemental Table 5.

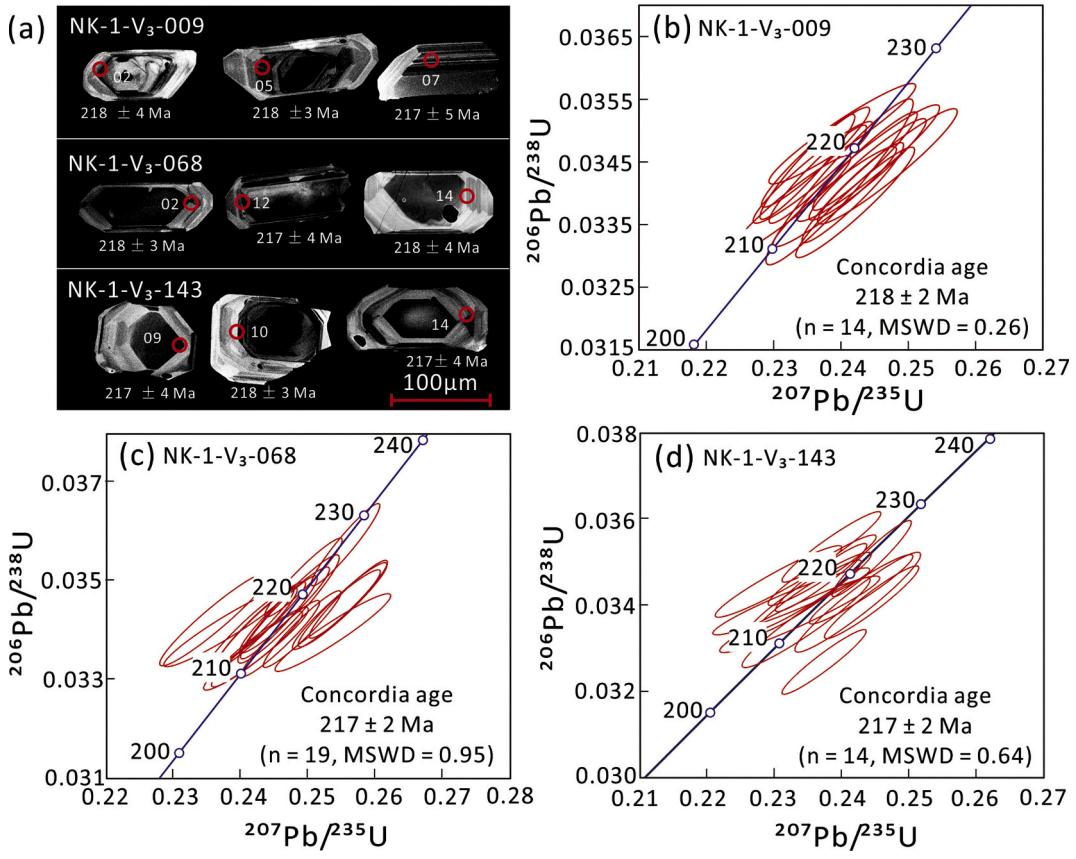


**Fig. 3.** (a) Representative CL images of zircons in dacites from Well NK-1. (b–d) Zircon U—Pb concordia diagrams for dacites from Well NK-1.

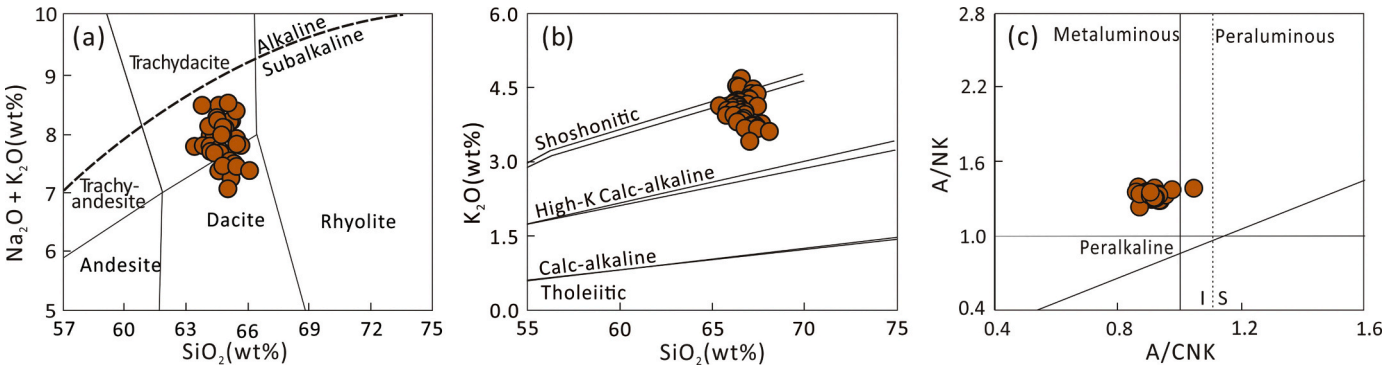


**Fig. 5.** (a) Total alkalis–silica classification diagram (data were corrected on a volatile-free basis; Le Maitre, 1989). (b) $K_2O$ vs. $SiO_2$. (c) A/NK vs. A/CNK.

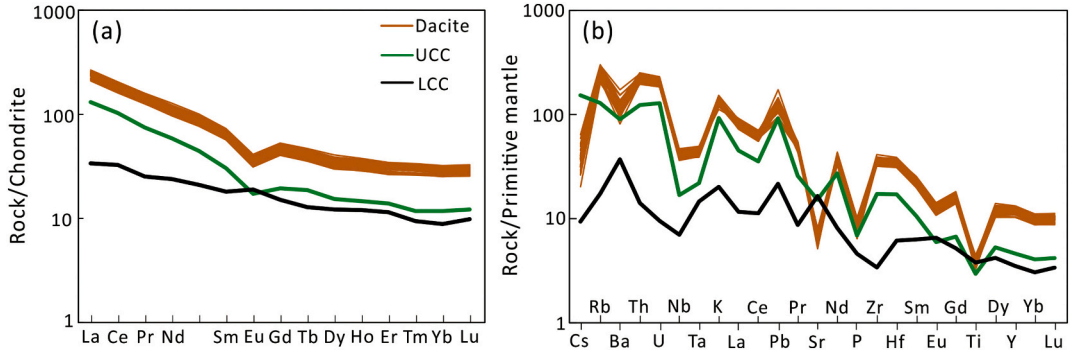


**Fig. 6.** (a) Chondrite-normalized REE patterns and (b) primitive mantle-normalized trace element diagrams for dacites from Well NK-1. Normalization values were taken from Sun and McDonough (1989), and UCC and LCC data are from Rudnick and Gao (2003).

The initial $(^{87}Sr/^{86}Sr)_i$, $(^{206}Pb/^{204}Pb)_i$, $(^{207}Pb/^{204}Pb)_i$, and $(^{208}Pb/^{204}Pb)_i$ ratios and $\varepsilon_{Nd}(t)$ and $\varepsilon_{Hf}(t)$ values were recalculated at 217 Ma.

The dacites have slightly variable $^{87}Sr/^{86}Sr$ (0.71767–0.72257), but uniform $^{143}Nd/^{144}Nd$ and $^{176}Hf/^{177}Hf$ ratios (0.51221–0.51223 and 0.28261–0.28264, respectively), which correspond to high $(^{87}Sr/^{86}Sr)_i$ ratios (0.70976–0.71094) and negative $\varepsilon_{Nd}(t)$ (−6.2 to −4.8) and $\varepsilon_{Hf}(t)$ values (−2.7 to −1.8; Fig. 7a–b). Two-stage Nd model ages ($T_{2DM}$) are relatively old (1.5–1.4 Ga). The dacites have uniform Pb isotopic

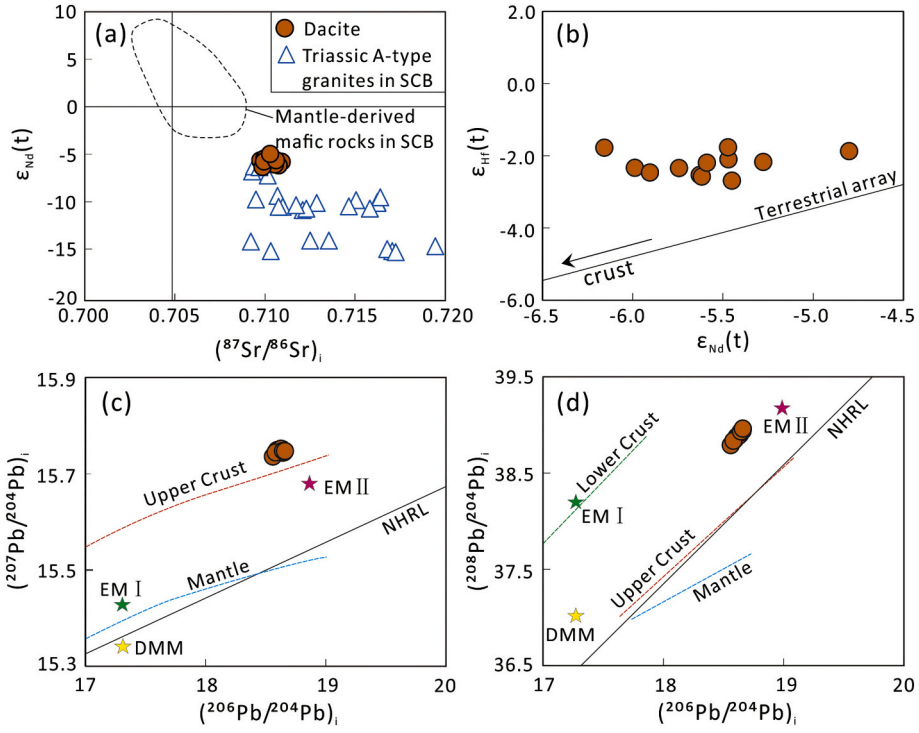


**Fig. 7.** Sr–Nd–Hf–Pb isotope data for dacites from Well NK-1. (a) $\varepsilon_{Nd}$ vs. $(^{87}Sr/^{86}Sr)_i$; (b) $\varepsilon_{Hf}(t)$ vs. $\varepsilon_{Nd}(t)$; (c) $(^{207}Pb/^{204}Pb)_i$ vs. $(^{206}Pb/^{204}Pb)_i$; (d) $(^{208}Pb/^{204}Pb)_i$ vs. $(^{206}Pb/^{204}Pb)_i$. Data for Triassic A-type granites in the SCB are from Wang et al. (2005), Sun et al. (2011), and Zhao et al. (2013). The Nd—Hf isotopic terrestrial array ($\varepsilon_{Hf} = \varepsilon_{Nd} \times 1.59 + 1.28$) is from Chauvel et al. (2008). Data for DM, EMI, and EMII are from Workman and Hart (2005) and Iwamori and Nakamura (2015). The Northern Hemisphere Reference Line (NHRL) is from Hart (1984). The reference lines for upper crust, lower crust, and mantle in (c) and (d) are from Zartman and Haines (1988).

compositions ($^{206}Pb/^{204}Pb$ = 19.040–19.156; $^{207}Pb/^{204}Pb$ = 15.762–15.774; $^{208}Pb/^{204}Pb$ = 39.487–39.643), corresponding to slightly variable initial $(^{206}Pb/^{204}Pb)_i$, $(^{207}Pb/^{204}Pb)_i$, and $(^{208}Pb/^{204}Pb)_i$ ratios of 18.565–18.664, 15.736–15.752, and 38.791–38.962, respectively (Fig. 7c–d).

## 4. Discussion

### 4.1. Fractional crystallization

The dacites are porphyritic and contain abundant phenocrysts of plagioclase, biotite, and titanite (Fig. 2), suggesting that their parental magmas underwent fractionation of these minerals. Biotite is an Al-rich mineral and has a high partition coefficient for Sc but a low partition coefficient for Th (Bea et al., 1994). Fractionation of biotite will increase $SiO_2/Al_2O_3$ and decrease Sc/Th ratios in residual melts. Thus, the negative correlation between Sc/Th and $SiO_2/Al_2O_3$ for the dacites (Fig. 8a) may indicate fractional crystallization of biotite, which is consistent with their low $Mg^{\#}$ values (19.2–31.7) that broadly decrease with increasing $SiO_2$ (Fig. 8b). Given that titanite has a lower partition coefficient for La than Sm, its fractionation will increase La/Sm ratios in the residual melt. Thus, the negative correlation between La/Sm and $TiO_2$ in the dacites denotes the fractional crystallization of titanite (Fig. 8c). Furthermore, the dacite samples all have negative Eu and Sr anomalies (Fig. 6), which may be due to fractional crystallization of plagioclase. The dacites would be primary low in Cr, Ni, and MgO for very low whole-rock Cr, Ni, and MgO contents and lack of any correlations between them (Fig. 8d–e).

### 4.2. Geochemical affinities with A-type granites

Granitoids are traditionally divided into M-, I-, S-, and A-types according to their source and geochemical characteristics (Chappell, 1999). The dacites from Well NK-1 have negative whole-rock $\varepsilon_{Nd}(t)$ and $\varepsilon_{Hf}(t)$ values, and low MgO, Cr, and Ni contents and Ce/Pb ratios (Fig. 8d–h). These features are inconsistent with M-type granites, which are generally formed by partial melting of juvenile-mantle-derived materials (Whalen et al., 1987). S-type granites typically have high $SiO_2$ contents (>72 wt%) and are strongly peraluminous with high A/CNK values (>1.1; Chappell, 1999), which is not the case for the dacites from Well NK-1 ($SiO_2$ < 68.1 wt%; A/CNK = 0.86–1.05; Supplemental Table 5). The geochemical characteristics of the studied samples

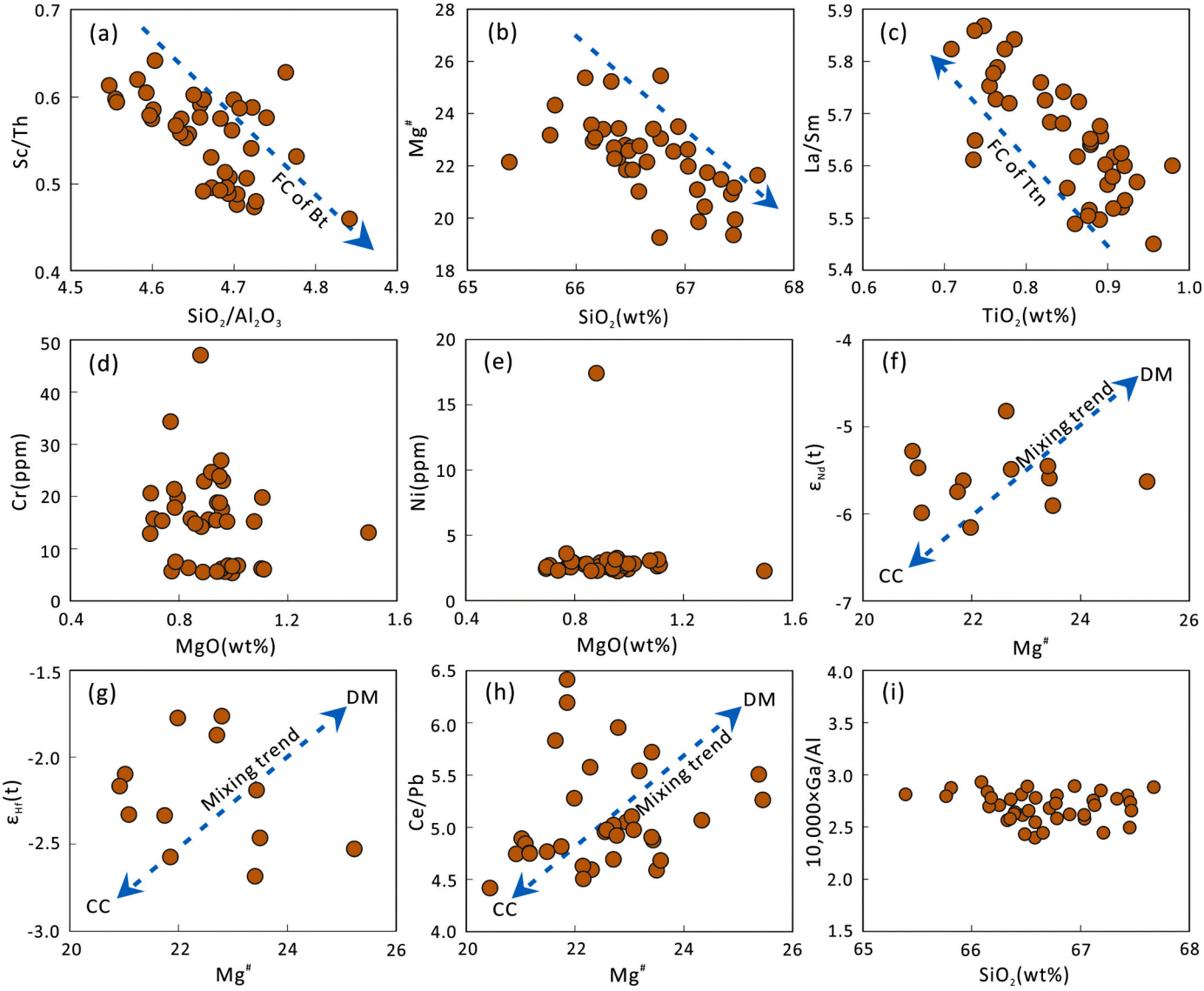


**Fig. 8.** Geochemical and isotopic plots for dacites from Well NK-1. (a) $Mg^{\#}$ vs. $SiO_2$; (b) Sc/Th vs. $SiO_2/Al_2O_3$; (c) La/Sm vs. $TiO_2$; (d) Cr vs. MgO; (e) Ni vs. MgO; (f) $\varepsilon_{Nd}(t)$ vs. $Mg^{\#}$; (g) $\varepsilon_{Hf}(t)$ vs. $Mg^{\#}$; (h) Ce/Pb vs. $Mg^{\#}$; (i) 10,000 × Ga/Al vs. $SiO_2$.

resemble those of A- and I-type granites; some highly fractionated I-type granites are geochemically similar to A-type granites (Whalen et al., 1987). The studied dacites have affinities with typical A-type granites, but are distinct from highly fractionated I-type granites due to: (a) their high total alkali ($Na_2O + K_2O$ = 7.39–8.42 wt%) and Zr + Ce + Nb + Y (530–680 ppm) contents, high $FeO^{Tot}/MgO$ ratios (5.22–7.48), and 10,000 × Ga/Al values (2.40–2.94; Supplemental Table 5; Fig. 9a–b), which are typical features of A-type granites (Eby, 1992; Whalen et al., 1987); (b) their relatively low $SiO_2$ contents (<68.1 wt%), which differ from highly fractionated I-type granites that usually have high $SiO_2$ contents (Whalen et al., 1987); (c) the absence of a linear relationship between 10,000 × Ga/Al and $SiO_2$ (Fig. 8i), indicating that the high Ga/Al ratios were not caused by extensive fractionation; and (d) their zircon saturation temperatures ($T_{Zr}$) (806–855 °C; mean = 830 °C) being higher than those of highly fractionated I-type granitoids (mean = 764 °C; King et al., 1997), but similar to those of Triassic A-type granites distributed along the NNE–SSW-trending Zhenghe–Dapu Fault in the SCB (Fig. 10a). A-type granites can be subdivided into $A_1$- and $A_2$-types, based on geochemical features such as Y/Nb ratios (Eby, 1992). The studied dacites are $A_2$-type granites (Fig. 9c–d), based on their Y and Nb concentrations and high Y/Nb ratios (1.7–1.9).

### 4.3. T–P–$fO_2$ conditions of melting

The geochemical composition of granitic magmas is mainly affected by the source materials. Furthermore, the temperature (King et al., 1997), pressure (depth) (Patiño Douce, 1997), and oxygen fugacity ($fO_2$) (Dall'Agnol and Oliveira, 2007) can also create different A-type granitic compositions.

The estimated zircon saturation temperatures can represent the lowest temperature of the primitive magma when the rocks lack inherited zircons (Chappell et al., 1998). The studied dacites have relatively high $T_{Zr}$ values of 806–855 °C (Fig. 10a) and provide a general estimate of the minimum temperature of the primitive melts to the studied dacites.

The compositions of plagioclase phenocrysts and host rocks in an albite-liquid equilibrium system can be used to estimate the pressure of magma chamber (Putirka, 2008), which might represent the minimum estimation of melting pressure. Thus, the calculated pressure of 8–10 kbar based on plagioclase and whole-rock composition (Supplemental Table 3) indicates the magma generation in the lower continental crust.

A-type granites can also be subdivided into reduced and oxidized types based on oxygen fugacity (Dall'Agnol and Oliveira, 2007). The studied dacites are characterized by moderate $FeO^{Tot}/(FeO^{Tot} + MgO)$ values (0.79–0.88) and most samples plot in the field for oxidized A-type granites (Fig. 10b), which is consistent with the estimation of oxygen fugacity (higher than the NNO buffer) based on the apatite compositions (Fig. 10c). Thus, the dacites from Well NK-1 formed in oxidized conditions.

### 4.4. Petrogenesis and magma source

A-type granites can be produced by fractional crystallization of mantle-derived basaltic melts (e.g., Litvinovsky et al., 2002), mixing between crust- and mantle-derived melts (e.g., Wickham et al., 1996), or partial melting of crustal sources (Whalen et al., 1987). The low MgO, Cr, and Ni contents of studied dacites (Fig. 8d–e) suggest a minimal or no mantle contribution. The samples do not contain mafic microgranular enclaves, and only have small variations in whole-rock geochemical compositions, with no correlations between $Mg^{\#}$ and $\varepsilon_{Nd}(t)$, $\varepsilon_{Hf}(t)$, and Ce/Pb (Fig. 8f–h). This precludes magma mixing between crust- and mantle-derived melts. Extensive fractional crystallization of a mantle-derived basaltic melt generally produces peralkaline magmas (Patiño Douce, 1997), which are obviously different from the metaluminous nature of the studied dacites (Fig. 5c). In addition, the dacites are characterized by high $(^{87}Sr/^{86}Sr)_i$ ratios and low $\varepsilon_{Nd}(t)$ and $\varepsilon_{Hf}(t)$ values, which are different from young mantle-derived mafic igneous rocks (Fig. 7a–b). Halogen contents in apatite can be used to estimate the volatile concentrations of the melt prior to ascent and degassing (Jiang et al., 2018). Based on apatite–melt partition coefficients for F in

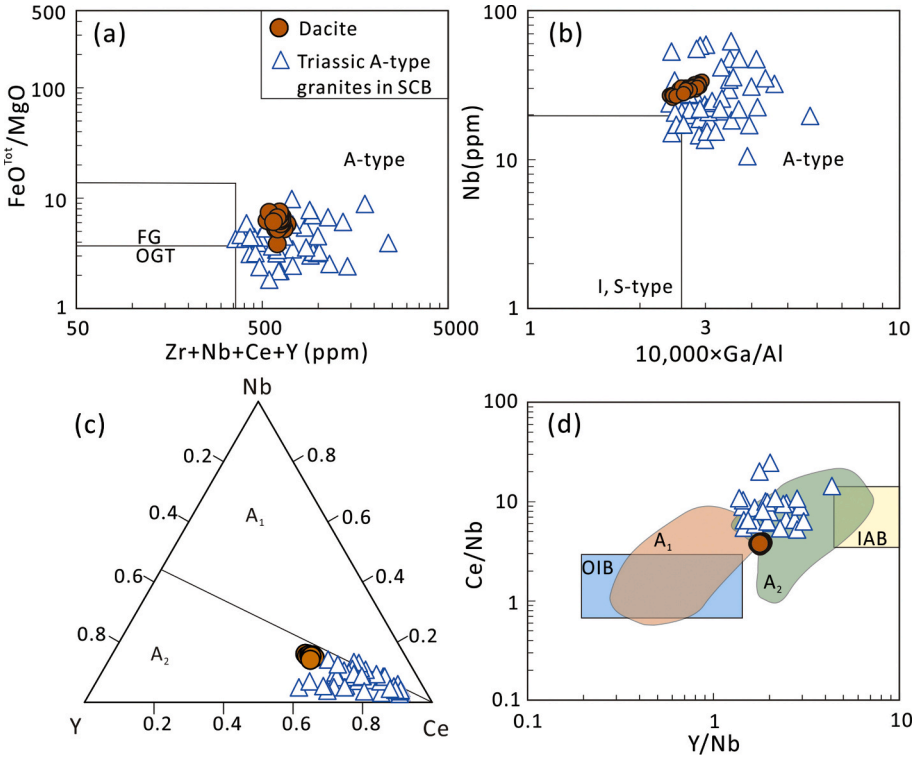


**Fig. 9.** Geochemical discrimination diagrams for dacites from Well NK-1. (a) ($FeO^{Tot}/MgO$) vs. (Zr + Nb + Ce + Y) (Whalen et al., 1987); (b) Nb vs. 10,000 × Ga/Al (Whalen et al., 1987); (c) Nb–Y–Ce (Eby, 1992); (d) Ce/Nb vs. Y/Nb (Eby, 1992).

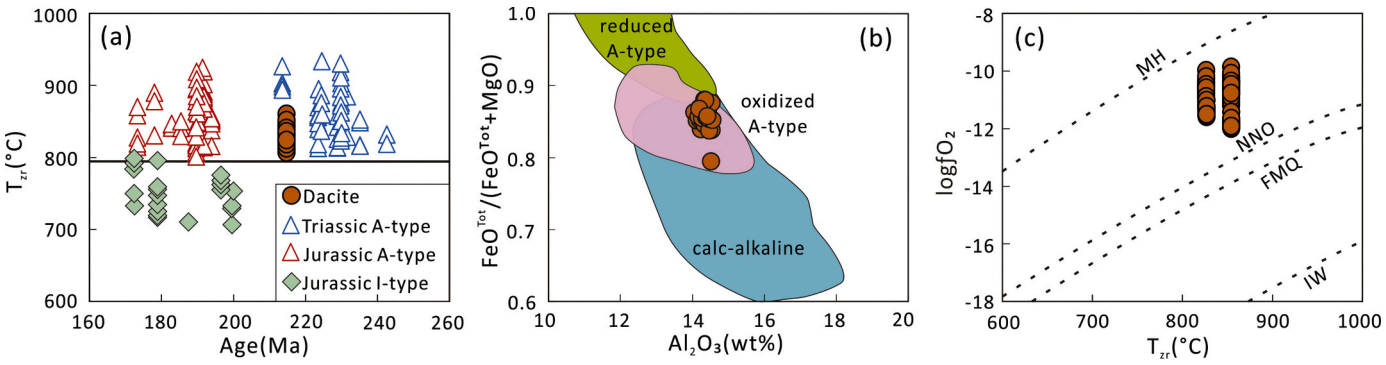


**Fig. 10.** (a) Zircon saturation temperatures ($T_{Zr}$) for dacites from Well NK-1 and Triassic–Jurassic A- and I-type granites in the SCB; the data for the Triassic–Jurassic A-type granites and Late Permian–Early Triassic syenites, and Jurassic I-type granites are the same as for Fig. 1; (b) diagram of $FeO^{Tot}/(FeO^{Tot} + MgO)$ vs. $Al_2O_3$; the fields of oxidized and reduced A-type granites are from Dall'Agnol and Oliveira (2007), and the field of calc-alkaline granites is from Frost et al. (2001); and (c) diagram of $\log fO_2$ vs. $T_{Zr}$ showing the oxygen fugacities (based on apatite composition) of the dacites from Well NK-1.

rhyolitic and dacitic melts at a high oxygen fugacity above the NNO buffer ($D_F^{apatite/melt}$ = 12.7; Webster et al., 2009), the estimated F concentration of dacitic melt for the studied samples is up to 2675 ppm (Supplemental Table 4), which is much higher than those of the primitive mantle and oceanic island basalts (F = 26 ppm and 1150 ppm, respectively; McDonough and Sun, 1995). This might preclude an origin by partial melting of a mantle source. Alternatively, the studied dacites could have been derived by partial melting of a crustal source based on the following: (a) low MgO contents (0.70–1.50 wt%) and $Mg^{\#}$ values (19–32), similar to pure crustal melts (Rapp and Watson, 1995); (b) continental crust-like trace element patterns (Fig. 6b); and (c) high $(^{87}Sr/^{86}Sr)_i$, negative $\varepsilon_{Nd}(t)$ and $\varepsilon_{Hf}(t)$, and high Pb isotopic compositions, which are different from those of mantle source or mantle-derived rocks but close to those of continental crust and Triassic A-type granites along the Zhenghe–Dapu Fault in the SCB (Fig. 7). This is consistent with high F concentration of the dacitic melts, which would be produced by partial melting of F-rich lower crustal rocks (F = 553 ppm; Rudnick and Gao, 2003) rather than by partial melting of a F-poor mantle source. Modeling calculations show that 20%–30% partial melting of a mafic lower continental crust (LCC) can produce the trace element concentrations and patterns that match those of the studied dacites (Fig. 11). The studied samples have relatively old Nd model ages ($T_{DM2-Nd}$ = 1.5–1.4 Ga), further indicating a source consisting of ancient crustal materials. Therefore, the Late Triassic dacites in the Nansha Block may be the product of partial melting of ancient lower–middle continental crust.

In addition, the studied dacites have decoupled Nd—Hf isotopic compositions, with relatively lower $\varepsilon_{Nd}(t)$ than $\varepsilon_{Hf}(t)$ values (Fig. 7b). Due to the large partition coefficient of Lu in garnet compared with Sm, Nd, and Hf, residual garnet from crustal melting events can retain Lu, which over time produces a reservoir with high $^{176}Hf/^{177}Hf$ relative to $^{143}Nd/^{144}Nd$ (Green et al., 2000; Zheng et al., 2005). Therefore, melts derived from garnet-bearing residual assemblages may have high $^{176}Hf/^{177}Hf$ relative to $^{143}Nd/^{144}Nd$ (Zheng et al., 2005). Such a melt would be depleted in HREEs and might have adakitic features, because the partition coefficients for HREEs between garnet and melt are much higher than those for LREEs. However, the studied dacites have relatively high HREE contents and low Sr/Y ratios (2.05–3.25; Supplemental Table 5), which are inconsistent with adakitic melts derived from a source with residual garnet. In general, a meta-sedimentary rock is depleted in Zr and Hf and has a high Lu/Hf ratio (0.09–0.11; Eroğlu et al., 2013) due to the "zircon effect" (Patchett et al., 1984). Partial melting of such a source can also produce Nd—Hf isotope decoupling. The studied dacites are enriched in Zr and Hf (Fig. 6b) and have low Lu/Hf ratios (0.06–0.07; Supplemental Table 5), which are obviously distinct from those of a meta-sedimentary source. A mantle source previously metasomatized by melts from subducted sediments can also have a decoupled Nd—Hf isotopic composition due to the higher mobility of Nd than Hf during partial melting of the subducted sediments. Melts derived from such an enriched mantle source would inherit the decoupled Nd—Hf isotopic composition of their source. The studied dacites have high $Na_2O$ contents and low $Al_2O_3/(MgO + FeO^{Tot})$ ratios, similar to melts from a source consisting of meta-basalts (Fig. 12). Therefore, their decoupled Nd—Hf isotopic composition (Fig. 7b) might have been inherited from a basaltic crustal source that was, in turn, derived from a mantle wedge metasomatized by melts from subducted sediments.

In summary, the studied dacites have $A_2$-type granite affinities and were derived from partial melting of ancient basaltic materials in the lower–middle continental crust under relatively high-temperature and oxidized conditions.

### 4.5. Tectonic affinities of the Nansha Block and implications for the Mesozoic tectonic evolution of the continental margin of the SCB

If the Nansha Block was once located along the southern margin of the SCB, it would have been affected by the subduction of the Paleo-Pacific plate during the Mesozoic because: (a) the age of dacites (218–217 Ma) in the Nansha Block is approximately consistent with the age peak (ca. 228 Ma) of detrital zircons from the eastern Cathaysia

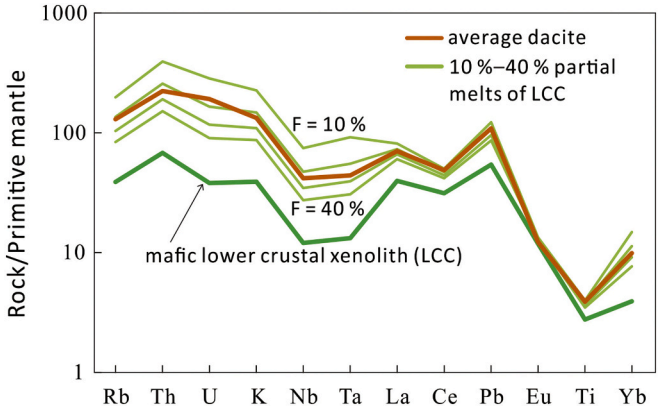


**Fig. 11.** Primitive-mantle-normalized multi-element patterns of the average dacite composition in Well NK-1, and batch partial melts of lower continental crust (represented by mafic lower crustal xenolith from the Qilin Cenozoic basalts in the Cathaysia Block). The residual mineralogy is plagioclase, clinopyroxene and orthopyroxene in the proportions of 0.51:0.30:0.19. The data and references for mafic lower crustal xenolith, and partition coefficients are given in Supplemental Table 6.

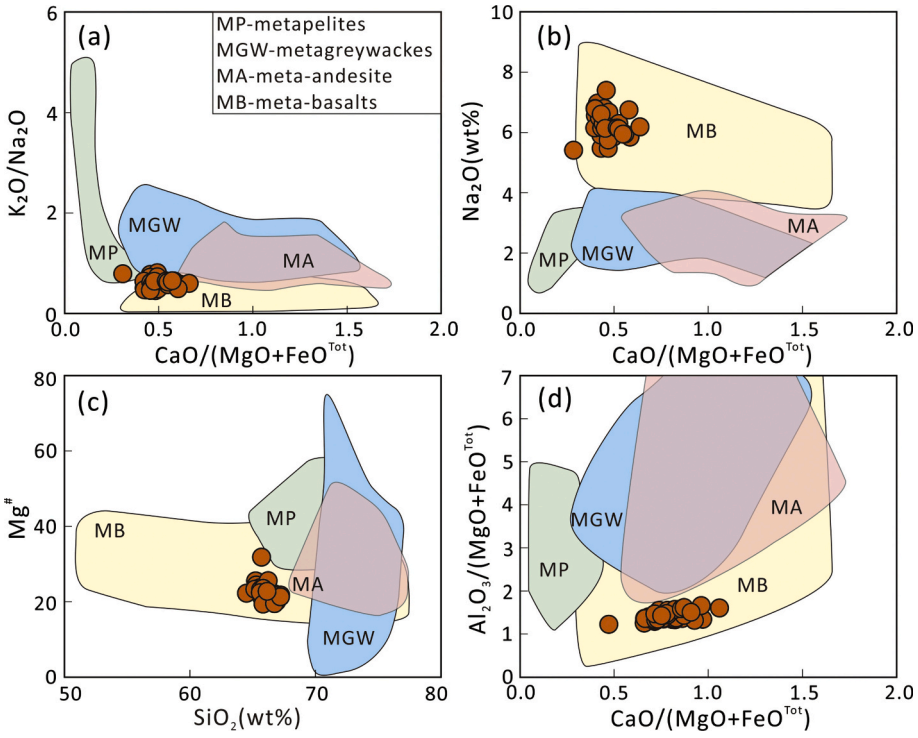


**Fig. 12.** Plots of (a) molar $K_2O/Na_2O$ vs. molar $CaO/(MgO + FeO^{Tot})$, (b) $Na_2O$ vs. molar $CaO/(MgO + FeO^{Tot})$, (c) $Mg^{\#}$ vs. $SiO_2$, and (d) molar $Al_2O_3/(MgO + FeO^{Tot})$ vs. molar $CaO/(MgO + FeO^{Tot})$ for dacites from Well NK-1. Also shown are results of partial melting experiments on crustal materials (i.e., meta-graywackes, meta-pelites, meta-andesite, and meta-basalt; Altherr and Siebel, 2002).

Block (Fig. 13a); (b) the studied dacites have similar geochemical features to Triassic A-type granites along the Zhenghe–Dapu Fault in the SCB (Sun et al., 2011; Wang et al., 2005; Zhao et al., 2013); (c) the two-stage Nd model ages ($T_{DM2-Nd}$) of the studied dacites (1.5–1.4 Ga) are close to those of Triassic granitoids in the SCB (2.0–1.4 Ga; Gao et al., 2017); (d) the surrounding blocks (e.g., the Reed Bank, Palawan, and Mindoro blocks) were attached to the continental margin of the SCB during the Mesozoic, based on their similar Mesozoic strata, gravity anomalies, P-wave velocity structures, and age peaks of detrital zircons (Almasco et al., 2000; Knittel et al., 2010; Kudrass et al., 1986; Shao et al., 2017; Suggate et al., 2014; Suzuki et al., 2000); (e) the Zhongsha, Xisha, and Nansha blocks must have been a united block due to their extremely similar Bouguer gravity anomalies (Zhu, 2019); and (f) Upper Triassic deltaic sandstones from the Nansha Block contain a Dictyophyllum–Clathropteris flora, which might have originated from the Cathaysia Block (Kudrass et al., 1986). Therefore, the petrogenesis of the studied Triassic dacites in the Nansha Block, which were coeval with A-type granites that occur along the Zhenghe–Dapu Fault in the SCB (246–215 Ma; Fig. 1a), provide significant insights into the tectonic evolution of the SCB during the Triassic.

A-type granites usually form in an extensional setting (Eby, 1992). There are two geodynamic models for the generation of Triassic A-type granites along the Zhenghe–Dapu Fault (246–215 Ma; Fig. 1a): (a) an extensional setting related to a far-field effect caused by collision between the SCB and Indochina or North China blocks (Zhao et al., 2013); and (b) strike-slip faulting related to oblique subduction of the Paleo-Pacific plate beneath the SCB (Sun et al., 2011; Wang et al., 2005). The former model is unlikely because the effect is difficult to propagate into the coastal area of the SCB. The NNE-trending distribution of the Triassic A-type granites and major faults in the coastal area of the SCB (Fig. 1a) is inconsistent with the collision of the SCB with the Indochina/North China blocks, which may produce EW-trending strike-slip faults and NE-trending local extensional faults (Zhao et al., 2013). In addition, the timing of continental collision of the SCB with the North China Block in the north (240–220 Ma; Zheng et al., 2009) and with the Indochina Block in the south (258–230 Ma; Hou et al., 2019) overlaps with the age of the studied dacites and A-type granites (246–215 Ma) along the Zhenghe–Dapu Fault (246–215 Ma; Fig. 1a), which is also inconsistent with an extensional tectonic setting for generation of the A-type granites (Eby, 1992). On the other hand, the emplacements of the Tieshan and Yangfang alkaline syenites in eastern Cathaysia (254–242 Ma) probably denote a transitional environment from compressional setting to extensional setting during the Late Permian–Early Triassic (Wang et al., 2005). Indeed, the studied dacites and A-type granites along the Zhenghe–Dapu Fault plot mostly within the within-plate granite field on diagrams of Rb vs. Y + Nb and Nb vs. Y (Fig. 14). Furthermore, the studied dacites have affinities with $A_2$-type granites (Fig. 9c–d) based on Y and Nb contents. The $A_2$-type granites might represent magmas derived from continental crust or underplated crust that has been through a cycle of continent-continent collision or island-arc magmatism (Eby, 1992), which is consistent with the source of ancient basaltic materials in the lower–middle continental crust for the studied dacites.

Some older mafic igneous rocks in the SCB (e.g., the Darongshan mafic rocks at 250–248 Ma and Hainan Island gabbroic–dioritic rocks at 256–245 Ma;Shen et al., 2018; Xu et al., 2018) geochemically resemble typical island arc basalts. These rocks are enriched in Rb, Th, U, and LREEs, depleted in Nb, Ta, and Ti, and have enriched Nd—Hf isotopic signatures, and likely formed in a back-arc setting caused by oblique subduction of the Paleo-Pacific plate beneath the SCB (Shen et al., 2018; Xu et al., 2018). Numerous NNE–SSW-trending, left-lateral, strike-slip faults in the Cathaysia Block, such as the Changle–Nan'ao and Zhenghe–Dapu faults (Fig. 1a), have been interpreted as the result of an extensional setting related to the oblique subduction of the Paleo-Pacific plate beneath the SCB that began in the Triassic or Late Permian (e.g., Li and Li, 2007; Wang et al., 2005; Zhou and Li, 2000). If this was the case, then the studied dacites and A-type granites and syenites along the Zhenghe–Dapu Fault formed in an extensional setting controlled by the WNW-directed subduction of the Paleo-Pacific plate (Sun et al., 2011; Wang et al., 2005).

There was a continental arc along the southeastern continental

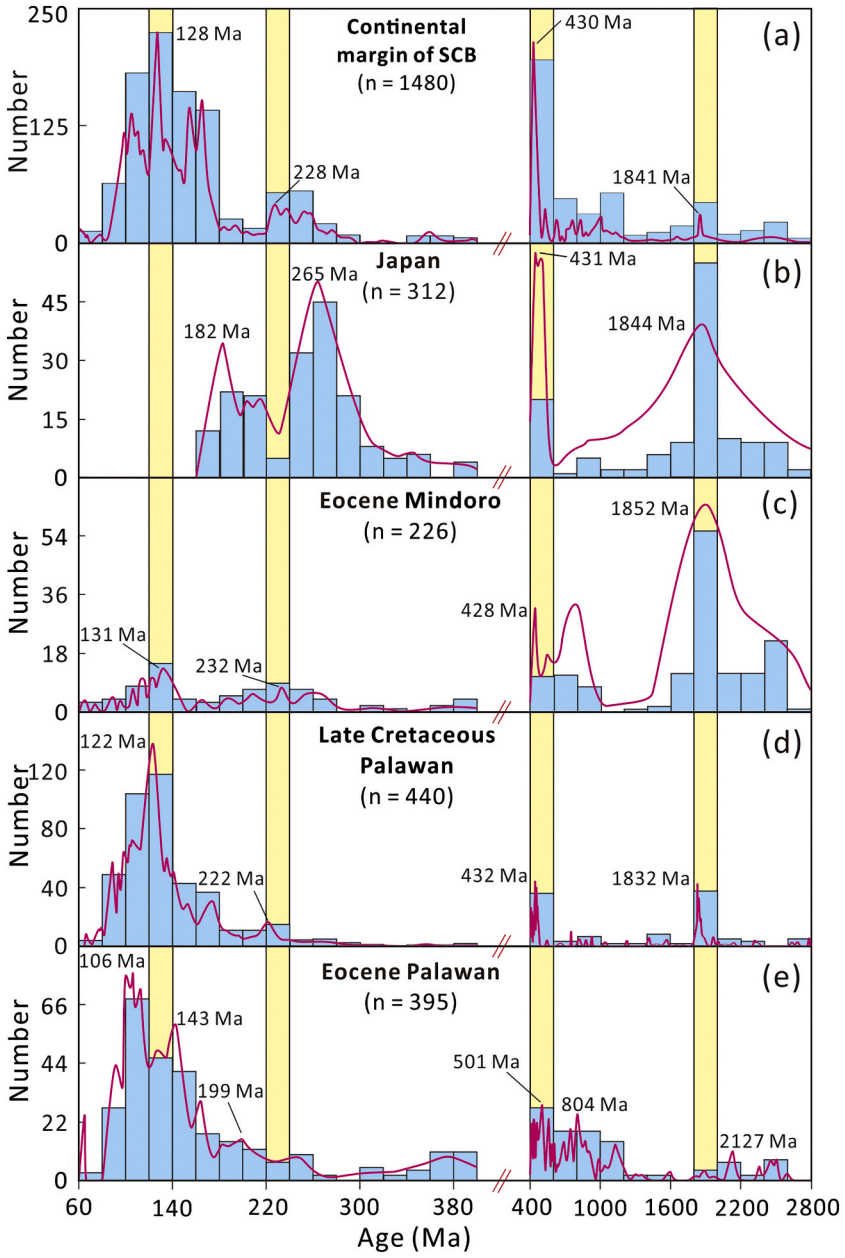


**Fig. 13.** Histograms of detrital zircon U—Pb ages of sedimentary rocks. Zircon U—Pb ages and data sources are given in Supplemental Table 7.

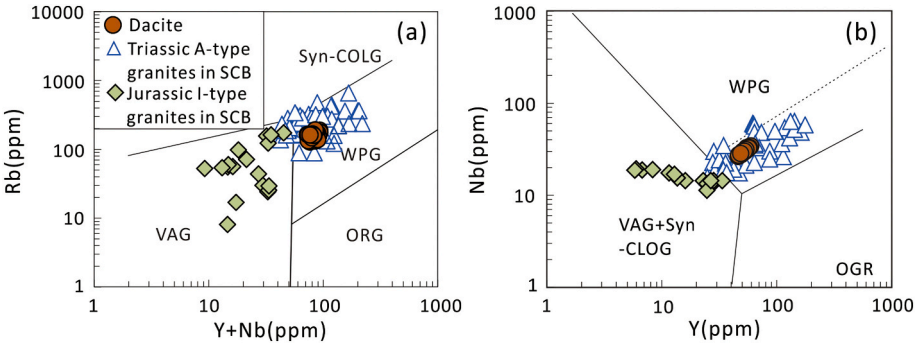


**Fig. 14.** Tectonic setting discrimination diagrams (Pearce et al., 1984) of (a) Rb vs. Yb + Nb, and (b) Nb vs. Y for dacites from Well NK-1. The data sources for the Triassic A-type granites are the same as for Fig. 1.

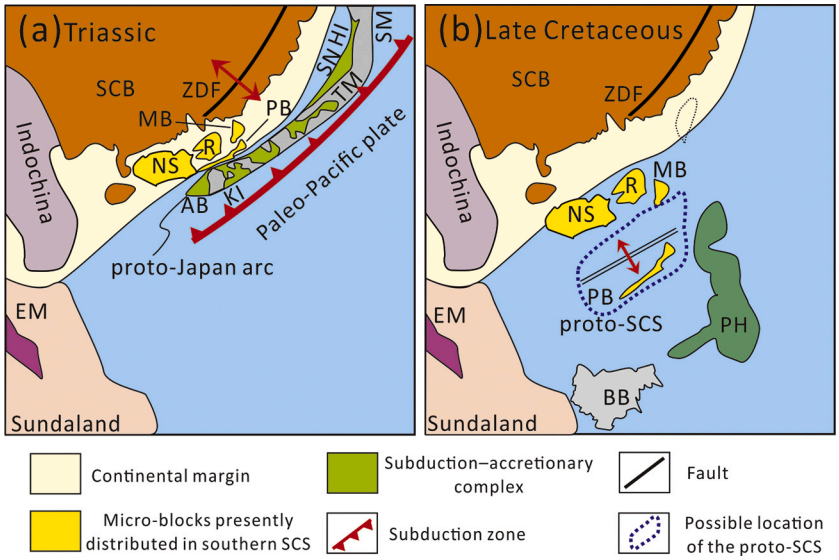


**Fig. 15.** (a) Triassic and (b) Late Cretaceous paleogeographic reconstructions of Southeast Asia. Abbreviations: Abukuma metamorphic complex (AB); Hida metamorphic complex (HI); Kitakami subduction–accretionary complex (KI); Samarka subduction–accretionary complex (SM); Sangun subduction–accretionary complex (SN); Tokoro subduction–accretionary complex (TM); Borneo Block (BB); Mindoro Block (MB); Nansha Block (NS); Palawan Block (PB); Philippines (PH); Reed Bank (R); Zhenghe–Dapu Fault (ZDF).

margin of the SCB during the Mesozoic. However, arc magmatism has not yet been clearly identified along the coastal area of the SCB. Instead, a proto-Japan arc outboard of the SCB (Fig. 15a) has been proposed for the following reasons: (a) most Mesozoic granitoids in southwest Japan are geochemically similar to Mesozoic granitoids in the SCB (including Taiwan), with high initial $^{87}Sr/^{86}Sr$ ratios, negative $\varepsilon_{Nd}(t)$ values, and Proterozoic Nd model ages (Jahn, 2010); (b) detrital zircons from Jurassic accretionary complexes in southwest Japan have Paleoproterozoic (ca. 1844 Ma) and Silurian (ca. 431 Ma) age peaks (Fig. 13b), similar to those from the continental margin of the SCB (ca. 1841 and 430 Ma; Fig. 13a) and "tonalities" from the Kurosegawa Belt in southwest Japan that contain abundant Meso- to Neoproterozoic zircons (1350–700 Ma; Aoki et al., 2015), which all suggest that the basement of southwest Japan has a SCB origin (Mizutani and Kojima, 1992); (c) some Permian–Jurassic subduction–accretionary complexes distributed along the Akiyoshi, Abukuma, Kitakami, and Tokoro belts in southwest Japan likely formed along the eastern margin of the SCB (Fig. 15a; Hara et al., 2018; Li et al., 2019); and (d) the corals in Middle Silurian strata in southwest Japan and Permian plants in central Japan all have an SCB origin (Cocks and Torsvik, 2013). In addition, detrital zircons from the Shikoku Belt in southwest Japan contain a dominant late Permian zircon population (ca. 265 Ma; Fig. 13b), which are interpreted to represent arc magmatism caused by the Paleo-Pacific plate subduction (Hara et al., 2018; Zhang et al., 2018). Thus, we propose that a proto-Japan arc existed in the trench–arc–basin system that was related to the WNW-directed subduction of the Paleo-Pacific plate during the early Mesozoic (Fig. 15a). The Wuzhishan granites (267–262 Ma) on Hainan Island are the product of continental arc magmatism related to Paleo-Pacific plate subduction in the late Permian (Li et al., 2006). Therefore, Paleo-Pacific plate subduction beneath the SCB restarted prior to the Early Triassic.

### 4.6. *Tectonic reconstruction of the SCS and its surrounding blocks*

The SCS is surrounded by the SCB to the north, the Borneo Block to the south, the Indochina Block to the west, and the Palawan and Mindoro blocks to the east (Fig. 1a). The widespread Mesozoic magmatism along the northern SCS margin was related to the Paleo-Pacific plate subduction (Xu et al., 2017), indicating a genetic relationship between the northern SCS margin and the SCB during the Mesozoic. This study shows that the southern SCS margin was also tectonically affiliated with the SCB and might also be dominated by the Paleo-Pacific plate subduction during the early Mesozoic, which provides more detailed insights into the tectonic evolution and paleogeography of East Asia since the Mesozoic.

During the Triassic, the SCB and Indochina Block separated from the Gondwana margin and then collided and were sutured together due to closure of the eastern Paleo-Tethys Ocean (Cocks and Torsvik, 2013). The studied dacites along the southern SCS margin formed in an extensional setting as a far-field effect related to the Paleo-Pacific plate subduction beneath the outboard proto-Japan arc in the Triassic (Fig. 15a). In addition, the studied dacites are likely related to the Triassic A-type granites distributed along the Zhenghe–Dapu Fault, indicating that the Nansha Block was part of the continental margin of the SCB in the Triassic. On the other hand, detrital zircons from the Eocene Lasala Formation (Mindoro Block) and Late Cretaceous Boayan Group and Guinlo Formation (Palawan Block) all show Paleoproterozoic (ca. 1852 and 1832 Ma), Silurian (ca. 428 and 432 Ma), and Triassic (ca. 232 and 222 Ma) age peaks that are similar to the continental margin of the SCB (Fig. 13c–d; Suggate et al., 2014; Shao et al., 2017). Paleomagnetic data show that the Mindoro and Palawan blocks had similar paleolatitudes to the SCB in the Jurassic–Cretaceous (e.g., Almasco et al., 2000), further indicating that these blocks might have been attached to the SCB during or prior to the Jurassic. In addition, the lithological unconformity in the SCB and the Reed Bank Block (Holloway, 1982) and similarity of P-wave velocity structures in the Reed Bank and Zhongsha blocks (Wei et al., 2015) indicate that the Reed Bank Block once occupied a pre-drift position within the SCB. Thus, the southern SCS continental margin that consists of the Nansha, Reed Bank, Palawan, and Mindoro blocks was located along the continental margin of the SCB and controlled by the subduction of the Paleo-Pacific plate beneath the proto-Japan arc in the early Mesozoic (Fig. 15a).

During the Cretaceous, the SCB continental margin was also controlled by the subduction of the Paleo-Pacific plate until subduction ceased and continental rifting began in the Late Cretaceous (Morley, 2016). It is notable that detrital zircons from the Late Cretaceous Boayan Group and Guinlo Formation in the Palawan Block have Paleoproterozoic (ca. 1832 Ma), Silurian (ca. 432 Ma), Triassic (ca. 222 Ma), and Cretaceous (ca. 122 Ma) age peaks similar to the continental margin of the SCB (Fig. 13d). In contrast, detrital zircons from the Eocene Panas Formation in the Palawan Block record episodic magmatism in the Neoproterozoic (ca. 804 Ma), Late Cambrian (ca. 501 Ma), and Cretaceous (143 and 106 Ma), which differ from the continental margin of the SCB (Fig. 13e). Therefore, the Palawan Block was connected with the continental margin of the SCB before the Late Cretaceous, and then drifted southeastward because of the opening of the proto-SCS during

the Late Cretaceous to Eocene (Morley, 2016; Zahirovic et al., 2014) (Fig. 15b). However, the Nansha, Mindoro, and Reed Bank blocks were still attached to the SCB during the Cretaceous (Fig. 15b) because: (a) the northern proto-SCS northwardly subducted beneath the Nansha Block during the Oligocene–Miocene (Wu and Suppe, 2018); (b) detrital zircons from the Eocene Lasala Formation in the Mindoro Block have Paleoproterozoic (ca. 1852 Ma), Silurian (ca. 428 Ma), Triassic (ca. 232 Ma), and Cretaceous (ca. 131 Ma) age peaks, which are similar to the continental margin of the SCB (Fig. 13c); and (c) the Reed Bank Block was likely located to the continental margin of the SCB before the Oligocene based on the magnetic anomalies of oceanic crust in the SCS basin (Briais et al., 1993; Li and Song, 2012).

## 5. Conclusions

(1) Dacites recovered from Well NK-1 in the Nansha Block in the SCS were emplaced during the Late Triassic (218–217 Ma) and have geochemical affinities with $A_2$-type granites. The dacites are products of the partial melting of lower–middle continental crust under high-temperature and oxidized conditions.
(2) The dacites from Well NK-1 and Triassic A-type granites along the Zhenghe–Dapu Fault formed in an extensional setting as a far-field effect of the Paleo-Pacific plate subduction beneath the outboard proto-Japan arc, which began before the Early Triassic.
(3) The southern margin of the present SCS was part of the continental margin of the SCB in the early Mesozoic, and was controlled by the subduction of the Paleo-Pacific plate. Most of blocks in the southern SCS continental margin were affiliated with the SCB during the Cretaceous except for the Palawan Block drifting southeastward in Late Cretaceous.

Supplementary data to this article can be found online at https://doi.org/10.1016/j.lithos.2021.106337.

## Declaration of Competing Interest

The authors declare that they have no known competing financial interests or personal relationships that could have appeared to influence the work reported in this paper.

## Acknowledgments

We thank L. Zhang, S.L. Sun, J.L. Ma, X.L. Tu and Y.N. Yang for analytical assistance. We are grateful to two anonymous reviewers for their careful reviews and constructive comments, and thank Prof. Xian-Hua Li for his editorial handling of this paper. This study was financially supported by the National Natural Science Foundation of China (NSFC Projects U1701641, 41625007, 41890812, 42021002), the Strategic Priority Research Program of the Chinese Academy of Sciences (XDA13010102), and the Key Special Project for Introduced Talents Team of Southern Marine Science and Engineering Guangdong Laboratory (Guangzhou) (GML2019ZD0202). This is contribution No. IS-3043 from GIG-CAS.

## References

Almasco, J.N., Rodolfo, K., Fuller, M., Frost, G., 2000. Paleomagnetism of Palawan, Philippines. J. Asian Earth Sci. 18, 369–389. https://doi.org/10.1016/S1367-9120(99)00050-4.
Altherr, R., Siebel, W., 2002. I-type plutonism in a continental back-arc setting, Miocene granitoids and monzonites from the Central Aegean Sea, Greece. Contrib. Mineral. Petrol. 143, 397–415. https://doi.org/10.1007/s00410-002-0352-y.
Aoki, K., Isozaki, Y., Yamamoto, A., Sakata, S., Hirata, T., 2015. Mid-Paleozoic arc granitoids in SW Japan with Neoproterozoic xenocrysts from South China: New zircon U-Pb ages by LA-ICP-MS. J. Asian Earth Sci. 97, 125–135. https://doi.org/10.1016/j.jseaes.2014.10.018.
Bea, F., Pereira, M.D., Stroh, A., 1994. Mineral/leucosome trace-element partitioning in a peraluminous migmatite (a laser ablation-ICP-MS study). Chem. Geol. 117 (1–4), 291–312. https://doi.org/10.1016/0009-2541(94)90133-3.
Briais, A., Patriat, P., Tapponnier, P., 1993. Updated interpretation of magnetic anomalies and seafloor spreading stages in the south china sea, implications for the tertiary tectonics of Southeast Asia. J. Geophys. Res. Solid Earth 98 (B4), 6299–6328. https://doi.org/10.1029/92JB02280.
Chappell, B.W., 1999. Aluminium saturation in I- and S-type granites and the characterization of fractionated haplogranites. Lithos 46, 535–551. https://doi.org/10.1016/S0024-4937(98)00086-3.
Chappell, B.W., Bryant, C.J., Wyborn, D., White, A.J.R., Williams, I.S., 1998. High and low temperature I-type granites. Resour. Geol. 48 (4), 225–235. https://doi.org/10.1111/j.1751-3928.1998.tb00020.x.
Chauvel, C., Lewin, E., Carpentier, M., Arndt, N.T., Marini, J.C., 2008. Role of recycled oceanic basalt and sediment in generating the Hf-Nd mantle array. Nat. Geosci. 1 (1), 64–67. https://doi.org/10.1038/ngeo.2007.51.
Chen, C.H., Lee, C.Y., Shinjo, R., 2008. Was there Jurassic paleo-Pacific subduction in South China, Constraints from 40Ar/39Ar dating, elemental and Sr-Nd-Pb isotopic geochemistry of the Mesozoic basalts. Lithos 106 (1), 83–92. https://doi.org/10.1016/j.lithos.2008.06.009.
Cocks, L.R.M., Torsvik, T.H., 2013. The dynamic evolution of the Palaeozoic geography of eastern Asia. Earth Sci. Rev. 117, 40–79. https://doi.org/10.1016/j.earscirev.2012.12.001.
Cullen, A., Reemst, P., Henstra, G., Gozzard, S., Ray, A., 2010. Rifting of the South ChinaSea: new perspectives. Pet. Geosci. 16, 273–282. https://doi.org/10.1144/1354-079309-908.
Dall'Agnol, R., Oliveira, D.C.D., 2007. Oxidized, magnetite-series, rapakivi-type granites of carajás, Brazil, implications for classification and petrogenesis of A–type granites. Lithos 93, 215–233. https://doi.org/10.1016/j.lithos.2006.03.065.
Dong, M., Zhang, J., Wu, S.G., Wang, B.Y., Ai, B.Y., 2019. Cooling of the lithosphere beneath the Nansha Block, South China Sea. J. Asian Earth Sci. 171, 169–177. https://doi.org/10.1016/j.jseaes.2018.06.007.
Eby, G.N., 1992. Chemical subdivision of the A-type granitoids, petrogenetic and tectonic implications. Geology 20, 641–644. https://doi.org/10.1130/0091-7613(1992)020<0641:CSOTAT>2.3.CO;2.
Eroğlu, S., Siebel, W., Danišík, M., Pfänder, J.A., Chen, F.K., 2013. Multi-system geochronological and isotopic constraints on age and evolution of the Gaoligongshan metamorphic belt and shear zone system in western Yunnan, China. J. Asian Earth Sci. 73, 218–239. https://doi.org/10.1016/j.jseaes.2013.03.031.
Frost, B.R., Barnes, C.G., Collins, W.J., Arculus, R.J., Ellis, D.J., Frost, C.D., 2001. A geochemical classification for granitic rocks. J. Petrol. 42, 2033–2048. https://doi.org/10.1093/petrology/42.11.2033.
Gao, P., Zheng, Y.F., Zhao, Z.F., 2017. Triassic granites in South China: a geochemical perspective on their characteristics, petrogenesis, and tectonic significance. Earth Sci. Rev. 173, 266–294. https://doi.org/10.1016/j.earscirev.2017.07.016.
Green, T.H., Blundy, J.D., Adam, J., Yaxley, G.M., 2000. SIMS determination of trace element partition coefficients between garnet, clinopyroxene and hydrous basaltic liquids at 2–7.5 GPa and 1080–1200 °C. Lithos 53, 165–187. https://doi.org/10.1016/S0024-4937(00)00023-2.
Hall, R., 2012. Late Jurassic-Cenozoic reconstructions of the Indonesian region and the Indian Ocean. Tectonophysics 570–571 (11), 1–41. https://doi.org/10.1016/j.tecto.2012.04.021.
Hara, H., Hiramo, M., Kurihara, T., Takahashi, T., Ueda, H., 2018. Permian arc evolution associated with Panthalassa subduction along the eastern margin of the South China block, based on sandstone provenance and U–Pb detrital zircon ages of the Kurosegawa belt, Southwest Japan. J. Asian Earth Sci. 151, 112–130. https://doi.org/10.1016/j.jseaes.2017.10.025.
Hart, S.R., 1984. A large-scale isotope anomaly in the southern hemisphere mantle. Nature 309, 753–757. https://doi.org/10.1038/309753a0.
Holloway, N.H., 1982. The North Palawan block, Philippines: its relation to the Asian mainland and its role in the evolution of the South China Sea. Geol. Soc. Malaysia Bull. 14, 19–58. https://doi.org/10.7186/bgsm14198102.
Hou, L., Xiong, F., Wang, W., Guo, L., Zhang, Q., 2019. Carboniferous-Triassic felsic igneous rocks and typical mineral deposits in the Truong Son orogenic belt, SE Asia: implications for Paleo-Tethyan tectonic evolution and metallogeny. Ore Geol. Rev. 112, 103036. https://doi.org/10.1016/j.oregeorev.2019.103036.
Huang, X.L., Niu, Y.L., Xu, Y.G., Qiu, H.N., Ma, J.L., Zhong, J.W., 2013. Geochronology and geochemistry of Cenozoic basalts from eastern Guangdong, SE China, constraints on the lithosphere evolution beneath the northern margin of the South China Sea. Contrib. Mineral. Petrol. 165 (3), 437–455. https://doi.org/10.1007/s00410-012-0816-7.
Iwamori, H., Nakamura, H., 2015. Isotopic heterogeneity of oceanic, arc and continental basalts and its implications for mantle dynamics. Gondwana Res. 27, 1131–1152. https://doi.org/10.1016/j.gr.2014.09.003.
Jahn, B.M., 2010. Accretionary orogen and evolution of the Japanese Islands, Implications from a Sr-Nd isotopic study of the Phanerozoic granitoids from SW Japan. Am. J. Sci. 310 (10), 1210–1249. https://doi.org/10.2475/10.2010.02.
Jiang, X.Y., Li, H., Ding, X., Wu, K., Guo, J., Liu, J.Q., Sun, W.D., 2018. Formation of A-type granites in the lower Yangtze River Belt, a perspective from apatite geochemistry. Lithos 304–307, 125–134. https://doi.org/10.1016/j.lithos.2018.02.005.
King, P.L., White, A.J.R., Chappell, B.W., Allen, C.M., 1997. Characterization and origin of aluminous A-type granites from the Lachlan Fold Belt. Southeastern Australia. J. Petrol. 38, 371–391. https://doi.org/10.1093/petroj/38.3.371.
Knittel, U., Hung, C.H., Yang, T.F., Iizuka, Y., 2010. Permian arc magmatism in Mindoro, the Philippines, an early Indosinian event in the Palawan Continental Terrane. Tectonophysics 493, 113–117. https://doi.org/10.1016/j.tecto.2010.07.007.
Kudrass, H.R., Wiedicke, M., Cepek, P., Muller, P., 1986. Mesozoic and Cainozoic rocks dredged from the South China Sea (Reed Bank area) and Sulu Sea and their

significance for plate–tectonic reconstructions. Mar. Pet. Geol. 3 (1), 19–30. https://doi.org/10.1016/0264-8172(86)90053-X.
Le Maitre, R.W., 1989. A Classification of Igneous Rocks and Glossary of Terms, Recommendation of the IOU Subcommission on the Systematics of Igneous Rocks. Blackwell, Oxford.
Li, Z.X., Li, X.H., 2007. Formation of the 1300-km-wide intracontinental orogen and post-orogenic magmatic province in Mesozoic South China, a flat-slab subduction model. Geology 35 (2), 179–182. https://doi.org/10.1130/G23193A.1.
Li, C.F., Song, T.R., 2012. Magnetic recording of the Cenozoic oceanic crustal accretion and evolution of the South China Sea basin. Chin. Sci. Bull. 57 (24), 3165–3181. https://doi.org/10.1007/s11434-012-5063-9.
Li, X.H., Li, Z.X., Li, W.X., Wang, Y.J., 2006. Initiation of the Indosinian orogeny in South China: evidence for a Permian magmatic arc on Hainan Island. J. Geol. 114 (3), 341–353. https://doi.org/10.1086/501222.
Li, J.H., Dong, S.W., Cawood, P.A., Zhao, G.C., Johnston, S.T., Zhang, Y.Q., Xin, Y.J., 2018. An Andean-type retro-arc foreland system beneath northwest South China revealed by SINOPROBE profiling. Earth Planet. Sci. Lett. 490, 170–179. https://doi.org/10.1016/j.epsl.2018.03.008.
Li, S.Z., Suo, Y.H., Li, X.Y., Zhou, J., Santosh, M., Wang, P.C., Wang, G.Z., Yu, S.Y., Lan, H.Y., Dai, L.M., Zhou, Z.Z., Cao, X.Z., Zhu, J.J., Liu, B., Jiang, S.H., Wang, G., Zhang, G.W., 2019. Mesozoic tectono-magmatic response in the east Asian ocean-continent connection zone to subduction of the Paleo-Pacific plate. Earth Sci. Rev. 192, 91–137. https://doi.org/10.1016/j.earscirev.2019.03.003.
Litvinovsky, B.A., Jahn, B.M., Zanvilevich, A.N., Saunders, A., Poulain, S., Kuzmin, D.V., 2002. Petrogenesis of syenite-granite suites from the Bryansky complex (Transbaikalia, Russia), implications for the origin of A-type granitoid magmas. Chem. Geol. 189, 105–133. https://doi.org/10.1016/S0009-2541(02)00142-0.
McDonough, W.F., Sun, S.S., 1995. The composition of the earth. Chem. Geol. 120, 223–253. https://doi.org/10.1016/0009-2541(94)00140-4.
Mizutani, S., Kojima, S., 1992. Mesozoic radiolarian biostratigraphy of Japan and collage tectonics along the eastern continental margin of Asia. Palaeogeogr. Palaeoclimatol. Palaeoecol. 96 (1–2), 3–22. https://doi.org/10.1016/0031-0182(92)90056-B.
Morley, C.K., 2016. Major unconformities/termination of extension events and associated surfaces in the South China Seas, review and implications for tectonic development. J. Asian Earth Sci. 120 (15), 62–86. https://doi.org/10.1016/j.jseaes.2016.01.013.
Patchett, P.J., White, W.M., Feldmann, H., Kielinczuk, S., Hofmann, A.W., 1984. Hafnium/rare earth element fractionation in the sedimentary system and crustal recycling into the Earth's mantle. Earth Planet. Sci. Lett. 69, 365–378. https://doi.org/10.1016/0012-821X(84)90195-X.
Patiño Douce, A.E., 1997. Generation of metaluminous A-type granites by low-pressure melting of calc-alkaline granitoids. Geology 25, 743–746.
Pearce, J.A., Harris, N.B.W., Tindle, A.G., 1984. Trace element discrimination diagrams for the tectonic interpretation of granitic rocks. J. Petrol. 25 (4), 956–983. https://doi.org/10.1093/petrology/25.4.956.
Putirka, D.K., 2008. Thermometers and Barometers for Volcanic Systems. Rev. Mineral. Geochem. 69, 61–120. https://doi.org/10.2138/rmg.2008.69.3.
Rapp, R.P., Watson, E.B., 1995. Dehydration melting of metabasalt at 8–32 kbar, implications for continental growth and crust-mantle recycling. J. Petrol. 36, 891–931. https://doi.org/10.1093/petrology/36.4.891.
Rudnick, R.L., Gao, S., 2003. Composition of the continental crust. Treatise Geochem. 3, 1–64. https://doi.org/10.1016/B978-0-08-095975-7.00301-6.
Shao, L., Cao, L., Qiao, P., Zhang, X., Li, Q., Van Hinsbergen, D.J.J., 2017. Cretaceous-Eocene provenance connections between the Palawan Continental Terrane and the northern South China Sea margin. Earth Planet. Sci. Lett. 477, 97–107. https://doi.org/10.1016/j.epsl.2017.08.019.
Shen, L.W., Yu, J.H., O'Reilly, S.Y., Griffin, W.L., Zhou, X.Y., 2018. Subduction-related middle Permian to early Triassic magmatism in Central Hainan Island, South China. Lithos 318–319, 158–175. https://doi.org/10.1016/j.lithos.2018.08.009.
Suggate, S.M., Cottam, M.A., Hall, R., Sevastjanova, I., Forster, M.A., White, L.T., Armstrong, R.A., Carter, A., Mojares, E., 2014. South China continental margin signature for sandstones and granites from Palawan, Philippines. Gondwana Res. 26, 699–718. https://doi.org/10.1016/j.gr.2013.07.006.
Sun, S.S., McDonough, W.F., 1989. Chemical and isotopic systematics of oceanic basalts, implications for mantle composition and processes. Geol. Soc. Lond., Spec. Publ. 42, 313–345. https://doi.org/10.1144/GSL.SP.1989.042.01.19.
Sun, Y., Ma, C.Q., Liu, Y.Y., She, Z.B., 2011. Geochronological and geochemical constraints on the petrogenesis of late Triassic aluminous A-type granites in Southeast China. J. Asian Earth Sci. 42 (6), 1117–1131. https://doi.org/10.1016/j.jseaes.2011.06.007.
Suo, Y.H., Li, S.Z., Jin, C., Zhang, Y., Zhou, J., Li, X.Y., Wang, C., Liu, Z., Wang, X.Y., Somervile, I., 2019. Eastward tectonic migration and transition of the Jurassic–cretaceous Andean-type continental margin along Southeast China. Earth Sci. Rev. 196, 102–884. https://doi.org/10.1016/j.earscirev.2019.102884.
Suzuki, S., Takemura, S., Yumul, G.P., David, S.D., Asiedu, D.K., 2000. Composition and provenance of the Upper cretaceous to Eocene sandstones in Central Palawan, Philippines, constraints on the tectonic development of Palawan. Island Arc 9, 611–626. https://doi.org/10.1111/j.1440-1738.2000.00306.x.
Wan, K.Y., Xia, S.H., Cao, J.H., Sun, J.L., Xu, H.L., 2017. Deep seismic structure of the northeastern South China Sea, Origin of a high-velocity layer in the lower crust. J. Geophys. Res. Solid Earth 122 (4), 2831–2858. https://doi.org/10.1002/2016jb013481.
Wang, Q., Li, J.W., Jian, P., Zhao, Z.H., Xiong, X.L., Bao, Z.W., Xu, J.F., Li, C.F., Ma, J.L., 2005. Alkaline syenites in eastern Cathaysia (South China), link to Permian-Triassic transtension. Earth Planet. Sci. Lett. 230 (3–4) https://doi.org/10.1016/j.epsl.2004.11.023, 339–354.
Wang, Y.J., Fan, W.M., Sun, M., Liang, X.Q., Zhang, Y.H., Peng, T.P., 2007. Geochronological, geochemical and geothermal constraints on petrogenesis of the Indosinian peraluminous granites in the South China Block, a case study in the Hunan Province. Lithos 96 (3–4), 475–502. https://doi.org/10.1016/j.lithos.2006.11.010.
Webster, J.D., Tappen, C.M., Mandeville, C.W., 2009. Partitioning behavior of chlorine and fluorine in the system apatite-melt-fluid. II, felsic silicate systems at 200 MPa. Geochim. Cosmochim. Acta 73, 559–581. https://doi.org/10.1016/j.gca.2008.10.034.
Wei, X.D., Ruan, A., Zhao, M.H., Qiu, X.L., Wu, Z.L., Niu, X.W., 2015. Shear wave velocity structure of Reed Bank, southern continental margin of the South China Sea. Tectonophysics 644–645, 151–160. https://doi.org/10.1016/j.tecto.2015.01.006.
Whalen, J.B., Currie, K.L., Chappell, B.W., 1987. A-type granites, geochemical characteristics, discrimination and petrogenesis. Contrib. Mineral. Petrol. 95, 407–419. https://doi.org/10.1007/BF00402202.
Wickham, S.M., Alberts, A.D., Zanvilevich, A.N., Litvinovsky, B.A., Bindeman, I.N., Schauble, E.A., 1996. A Stable Isotope Study of Anorogenic Magmatism in East Central Asia. J. Petrol. 37 (5), 1063–1095. https://doi.org/10.1093/petrology/37.5.1063.
Workman, R.K., Hart, S.R., 2005. Major and trace element composition of the depleted MORB mantle (DMM). Earth Planet. Sci. Lett. 231, 53–72. https://doi.org/10.1016/j.epsl.2004.12.005.
Wu, J., Suppe, J., 2018. Proto–South China Sea Plate tectonics using subducted slab constraints from tomography. J. Earth Sci. 29 (6), 1304–1318. https://doi.org/10.1007/s12583-017-0813-x.
Xu, C.H., Zhang, L., Shi, H.S., 2017. Tracing an early Jurassic magmatic arc from South to East China Seas. Tectonics 36, 466–492. https://doi.org/10.1002/2016TC004446.
Xu, W.C., Luo, B.J., Xu, Y.J., Wang, L., Chen, Q., 2018. Geochronology, geochemistry, and petrogenesis of late permian to early Triassic mafic rocks from Darongshan, South China, Implications for ultrahigh-temperature metamorphism and S-type granite generation. Lithos 308–309, 168–180. https://doi.org/10.1016/j.lithos.2018.03.004.
Yan, Q.S., Shi, X.F., Li, N.S., 2011. Oxygen and lead isotopic characteristics of granitic rocks from the Nansha Block (South China Sea), implications for their petrogenesis and tectonic affinity. Island Arc 20, 150–159. https://doi.org/10.1111/j.1440-1738.2010.00754.x.
Zahirovic, S., Seton, M., Müller, R.D., 2014. The cretaceous and Cenozoic tectonic evolution of Southeast Asia. Solid Earth Discuss. 5 (2), 1335–1422. https://doi.org/10.5194/se-5-227-2014.
Zartman, R., Haines, S., 1988. The plumbotectonic model for Pb isotopic systematics among major terrestrial reservoirs-a case for bidirectional transport. Geochim. Cosmochim. Acta 52, 1327–1339. https://doi.org/10.1016/0016-7037(88)90204-9.
Zhang, X.J., Takeuchi, M., Ohkawa, M., Matsuzawa, N., 2018. Provenance of a Permian accretionary complex (Nishiki Group) of the Akiyoshi Belt in Southwest Japan and Paleogeographic implications. J. Asian Earth Sci. 167, 130–138. https://doi.org/10.1016/j.jseaes.2018.01.005.
Zhao, K.D., Jiang, S.Y., Chen, W.F., Chen, P.R., Ling, H.F., 2013. Zircon U-Pb chronology and elemental and Sr-Nd-Hf isotope geochemistry of two Triassic A-type granites in South China, Implication for petrogenesis and Indosinian transtensional tectonism. Lithos 160–161, 292–306. https://doi.org/10.1016/j.lithos.2012.11.001.
Zheng, Y.F., Wu, Y.B., Zhao, Z.F., Zhang, S.B., Xu, P., Wu, F.Y., 2005. Metamorphic effect on zircon Lu-Hf and U-Pb isotope systems in ultrahigh-pressure ecologite-facies metagranite and metabasite. Earth Planet. Sci. Lett. 240, 340–378. https://doi.org/10.1016/j.epsl.2005.09.025.
Zheng, Y.F., Chen, R.X., Zhao, Z.F., 2009. Chemical geodynamics of continental subduction-zone metamorphism: insights from studies of the Chinese Continental Scientific Drilling (CCSD) core samples. Tectonophysics 475, 327–358. https://doi.org/10.1016/j.tecto.2008.09.014.
Zhou, X.M., Li, W.X., 2000. Origin of late Mesozoic igneous rocks in Southeastern China, implications for lithosphere subduction and underplating of mafic magmas. Tectonophysics 326 (3–4), 269–287. https://doi.org/10.1016/S0040-1951(00)00120-7.
Zhou, X.M., Sun, T., Shen, W.Z., Shu, L.S., Niu, Y.L., 2006. Petrogenesis of Mesozoic granitoids and volcanic rocks in South China, a response to tectonic evolution. Episodes 29 (1), 26–33. https://doi.org/10.1007/s00254-006-0175-7.
Zhu, Y.X., 2019. Geological-Geophysical Study Based on Gravity Magnetic Seismic Profile in South China Sea. Jilin University, Master's dissertation (In Chinese).